




RESEARCH ARTICLE

Extending the solid solution range of sodium ferric pyrophosphate: Off-stoichiometric $\text{Na}_3\text{Fe}_{2.5}(\text{P}_2\text{O}_7)_2$ as a novel cathode for sodium-ion batteries

Xiangjun Pu¹  | Kunran Yang¹  | Zibing Pan² | Chunhua Song^{3,4} | Yangyang Lai¹ | Renjie Li⁵ | Zheng-Long Xu⁵ | Zhongxue Chen²  | Yuliang Cao¹ 

¹Hubei Key Laboratory of Electrochemical Power Sources, College of Chemistry and Molecular Sciences, Wuhan University, Wuhan, China

²Key Laboratory of Hydraulic Machinery Transients, Ministry of Education, School of Power and Mechanical Engineering, Wuhan University, Wuhan, China

³School of Chemistry and Chemical Engineering, Jiangsu University of Technology, Changzhou, Jiangsu, China

⁴Zonergy Corporation, Zigong, Sichuan, China

⁵Department of Industrial and Systems Engineering, The Hong Kong Polytechnic University, Hung Hom, Hong Kong SAR, China

Correspondence

Chunhua Song, School of Chemistry and Chemical Engineering, Jiangsu University of Technology, Changzhou, Jiangsu 213001, China.

Email: song_chunhua@zonergy.com

Zhongxue Chen, Key Laboratory of Hydraulic Machinery Transients, Ministry of Education, School of Power and Mechanical Engineering, Wuhan University, Wuhan 430072, China.

Email: zxchen_pmc@whu.edu.cn

Yuliang Cao, Hubei Key Laboratory of Electrochemical Power Sources, College of Chemistry and Molecular Sciences, Wuhan University, Wuhan 430072, China.

Email: ylcao@whu.edu.cn

Funding information

National Natural Science Foundation of China, Grant/Award Numbers: 21972108, U20A20249, U22A20438; Changzhou Science and Technology Bureau, Grant/Award Number: CM20223017; Innovation and Technology Commission (ITC) of Hong Kong, The Innovation &

Abstract

Iron-based pyrophosphates are attractive cathodes for sodium-ion batteries due to their large framework, cost-effectiveness, and high energy density. However, the understanding of the crystal structure is scarce and only a limited candidates have been reported so far. In this work, we found for the first time that a continuous solid solution, $\text{Na}_{4-\alpha}\text{Fe}_{2+\alpha/2}(\text{P}_2\text{O}_7)_2$ ($0 \leq \alpha \leq 1$), could be obtained by mutual substitution of cations at center-symmetric Na3 and Na4 sites while keeping the crystal building blocks of anionic P_2O_7 unchanged. In particular, a novel off-stoichiometric $\text{Na}_3\text{Fe}_{2.5}(\text{P}_2\text{O}_7)_2$ is thus proposed, and its structure, energy storage mechanism, and electrochemical performance are extensively investigated to unveil the structure–function relationship. The as-prepared off-stoichiometric electrode delivers appealing performance with a reversible discharge capacity of 83 mAh g^{-1} , a working voltage of 2.9 V (vs. Na^+/Na), the retention of 89.2% of the initial capacity after 500 cycles, and enhanced rate capability of 51 mAh g^{-1} at a current density of 1600 mA g^{-1} . This research shows that sodium ferric pyrophosphate could form extended solid solution composition and promising phase is concealed in the range of $\text{Na}_{4-\alpha}\text{Fe}_{2+\alpha/2}(\text{P}_2\text{O}_7)_2$, offering more chances for exploration of new cathode materials for the construction of high-performance SIBs.

Xiangjun Pu and Kunran Yang contributed equally to this study.

This is an open access article under the terms of the [Creative Commons Attribution](https://creativecommons.org/licenses/by/4.0/) License, which permits use, distribution and reproduction in any medium, provided the original work is properly cited.

© 2023 The Authors. *Carbon Energy* published by Wenzhou University and John Wiley & Sons Australia, Ltd.

Technology Fund (ITF) with Project No. ITS/126/21

KEYWORDS

extending solid-solution range, off-stoichiometric $\text{Na}_3\text{Fe}_{2.5}(\text{P}_2\text{O}_7)_2$, sodium-ion batteries, structure–function relationship

1 | INTRODUCTION

The global shortage of lithium resources is hindering the development of lithium-ion batteries (LIBs) to support the long-term development of two major markets of electric vehicles and large-scale energy storage industries at the same time. Sodium-ion batteries (SIBs),^{1,2} which have rich resources and similar electro-chemistry to LIBs, are becoming one of the ideal choices for grid-level energy storage systems. At present, the specific capacity of a typical hard carbon anode can reach about 300 mAh g^{-1} or above by rational structure design,^{3,4} close to that of the commercial graphite anode for LIBs, enabling the commercialization of SIBs; however, the cathode material is the main bottleneck restricting long-term development because only limited intercalating hosts have been proposed so far.⁵

Sodium cathode materials mainly include transition-metal oxides (Na_xMO_2 , either layer or tunnel structure),^{5–8} Prussian blue analogs (PBAs),⁹ and polyanionic compounds.^{10–12} Although some recent reports demonstrated that layered Na_xMO_2 could show high capacity, they still have problems in terms of safety at high state of charge (SOC), irreversible phase transition (leading to poor structural stability), high cost (rare Ni, Cu, and Mn always incorporated), and even difficulty in storage caused by their hygroscopic nature.^{13,14} In addition, tunnel-structure Na_xMO_2 (where $x < 0.5$, with $\text{Na}_{0.44}\text{MnO}_2$ as the representative) is mainly hindered by low reversible initial capacity and inferior energy density.^{6,7} For PBAs, although the rigid open framework and large interstitial sites are beneficial for repeated Na^+ insertion/extraction, the degree of phase purity and crystallinity, as well as water content, have an adverse influence on the actual performance. Besides, the easily formed vacancies in PBAs often markedly shorten the cycling lifespan because they reduce the electronic conductivity, leading to skeleton collapse and lattice disorder.¹⁵ In comparison, polyanionic compounds are attractive cathodes owing to the open framework structure and good structural and thermal stability endowed by strong covalent bonds.^{16–18} Polyanionic compounds can be denoted as $\text{Na}_x\text{M}_y[(\text{X}_m\text{O}_n)^h]_z$, where M is a transition metal (like Fe, V, and Mn), and X is P, S, Si, and so on. Polyanionic cathodes, especially iron-redox centered phosphate and pyrophosphate, with advantages like abundant resources, cost-effectiveness, and an

environmentally friendly nature, have attracted extensive research interest.^{5,11,19}

Unlike the olivine LiFePO_4 with successful application in LIBs, the thermodynamically stable NaFePO_4 crystallizing in the maricite phase does not have feasible Na^+ diffusion channels and thus shows poor electrochemical capability. Though some researchers attempted to achieve sodium-storage activity, additional and complex measurements like extremely small nanodots²⁰ and unconventional ion exchange²¹ are required, which restricts its practical application. In addition, the large volume expansion (16.6%) between FePO_4 and sodiated NaFePO_4 is another unsolvable problem.²² Alternatively, sodium ferric pyrophosphate with strong inductive effect shows stable sodium-storage capability. Stoichiometric sodium ferric pyrophosphates ($\text{Na}_2\text{FeP}_2\text{O}_7$) were initially studied to develop a triclinic structure (space group: P-1) with three-dimensional channels running along [100], $[-110]$, and $[01-1]$ directions.²³ Later, Nazar et al. synthesized stoichiometric counterparts that can be extended to off-stoichiometric $\text{Na}_{4-\alpha}\text{Fe}_{2+\alpha/2}(\text{P}_2\text{O}_7)_2$ with $2/3 \leq \alpha \leq 7/8$.^{24,25} Very recently, a new sodium-rich $\text{Na}_{3.64}\text{Fe}_{2.18}(\text{P}_2\text{O}_7)_2$ compound was also explored as a cathode material for SIBs,²⁶ which actually yields α value of 0.36 if we include it in the general formula. Although previous studies attempted to examine the electrochemical activity of sodium ferric pyrophosphates, there were limitations in interpreting the crystal structure and only a few candidates have been reported so far. (1) The ferrite polyhedron configuration is erroneously interpreted to only include the $[\text{FeO}_6]$ octahedron in the $\text{Na}_{4-\alpha}\text{Fe}_{2+\alpha/2}(\text{P}_2\text{O}_7)_2$ crystal structure,^{27–31} and even the α value affects the occupancy of center-symmetric Na and Fe.²⁷ (2) Studies on kinetics and sodium storage behaviors are also incomplete. To the best of our knowledge, only one report attempted to identify the possible Na^+ diffusion channels by calculating the diffusion barrier using DFT.³² The results showed that there are only two feasible channels including the Na1 site one-dimensional (1D) pathway approximately parallel to the b axis and the Na2 site 1D pathway parallel to the bc plane in the structure.

In this work, aiming at extending the pyrophosphate chemistry for rechargeable Na-ion batteries, we report the synthesis and electrochemical characterization of off-stoichiometric $\text{Na}_3\text{Fe}_{2.5}(\text{P}_2\text{O}_7)_2$ (offsto-NFPO) as a novel Fe-based cathode, thus extending the

range of α value from previously reported $0.667 \leq \alpha \leq 0.875$ to $0 \leq \alpha \leq 1$, while maintaining crystal building blocks of P_2O_7 unchanged. Further deciphering of the structure shows that there is an edging-sharing $[\text{FeO}_4]$ tetrahedron and a third Na4 site 1D channel approximately perpendicular to the *ac* plane. More importantly, the offsto-NFPO shows improved sodium storage performance with excellent reversibility and enhanced stability without the necessity for nanosizing or complex carbon coating. This study provides a comprehensive analysis of the correlation between the structure–function relationship and provides new insights to exploit alternative cathodes of ferric pyrophosphate families for SIBs.

2 | EXPERIMENTAL SECTION

2.1 | Materials synthesis

Typically, both stoichiometric sto-NFPO and offsto-NFPO are synthesized using a simple and conventional ball-milling method, followed by a high-temperature solid-state reaction. In particular, stoichiometric amounts of $\text{NaAc} \cdot 3\text{H}_2\text{O}$, $(\text{NH}_4)_2\text{HPO}_4$, and $\text{FeC}_2\text{O}_4 \cdot 2\text{H}_2\text{O}$ were mixed using wet ball milling method at 300 rpm for 6 h in acetone, with sucrose as a carbon source added at the same time. Then, the mixture was placed in a drying chamber at 50°C to completely volatilize the dispersant and ground to obtain the precursors. Subsequently, precursors were treated by first calcinating in an Ar atmosphere at 300°C for 6 h to remove volatile constituents, and then ground and pelletized under a pressure of 10 MPa to decrease the solid reaction distance. Finally, it was again calcinated in an Ar atmosphere at 600°C for 12 h at a heating rate of 3°C min^{-1} , whereas cooling was allowed to proceed naturally to obtain the final in situ carbon-coated samples.

2.2 | Characterization

X-ray diffraction (XRD) measurements were recorded on a Bruker AXS diffractometer (D8 Advance) using $\text{Cu K}\alpha$ radiation at $\lambda = 1.54 \text{ \AA}$ at a scan rate of 2° min^{-1} . Scanning electron microscopy tests were carried out on a Hitachi S-4800 scanning electron microscope. The carbon content was determined on FlashSmart Organic Elemental Analyzers (Thermo Fisher Scientific). Inductively coupled plasma–optical emission spectrometry (ICP-OES) was performed on an Agilent730 (Agilent Technologies). All the structural illustrations were performed using VESTA software.³³

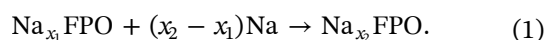
2.3 | Electrochemical measurements

The obtained offsto-NFPO composite was mixed with Super P and poly (vinylidene fluoride) (PVdF) in a mass ratio of 8:1:1, and the mixture was dispersed in *N*-methyl-2-pyrrolidone (NMP) to form a homogeneous slurry. Then, the slurry was cast on an Al foil and dried at 80°C for 10 h in a vacuum oven. Later, the electrode was punched with a loading of about 1.5 mg cm^{-2} and an area of 1.44 cm^2 . Electrochemical tests were performed on 2032 button cells with the above electrode as the cathode and Na metal as the counter electrode. The electrolyte was 1 mol L^{-1} NaClO_4 dissolved in a mixture of ethylene carbonate, diethyl carbonate, and fluoroethylene carbonate (1:1:0.05 by wt., Zhangjiagang Guotai-Huarong New Chemical Materials Co., Ltd.), and the separator was a microporous membrane (Celgard 2325). The coin cells were assembled in an Ar-filled glovebox with a water/oxygen content lower than 0.01 ppm. Galvanostatic charge and discharge were conducted on a CT2001A (Land Wuhan) battery tester with predischage, and cyclic voltammetric (CV) measurements performed on a CHI 660E electrochemical workstation (Chenhua).

2.4 | Density functional theory (DFT) calculation

First-principle calculations were performed using the Vienna ab initio simulation package within the periodic slabs. The generalized gradient approximation function developed by Perdew, Burke, and Ernzerhof was adopted in the calculation. The projector-augmented-wave method and a plane-wave basis set with a kinetic energy cut-off of 500 eV were used to determine the interaction between ions and electrons. The *k*-points were sampled on a grid of $3 \times 3 \times 1$ for the optimization of unit cell parameters, followed by geometry optimization using a $2 \times 2 \times 1$ *k*-point grid. Structures were relaxed until the force on each atom was no more than 0.05 eV \AA^{-1} , and the electronic self-consistent loop stopped until the total energy change between two steps was smaller than 10^{-4} eV . Initial spin moments were set to 4 for Fe to make the calculations tractable. Hubbard *U* correction was applied for the Fe 3d electrons, and according to a previous report, the effective *U* value was set as 4.3 eV.³⁴ The Na migration barrier energy was calculated using the climbing image nudged elastic band method (CI-NEB).

During the extraction/insertion of Na ions in the charge/discharge process, the concentration of sodium ions in the electrode will change as follows:



If we denote the total energy of $\text{Na}_{x_1}\text{FPO}$, Na , and $\text{Na}_{x_2}\text{FPO}$ calculated from DFT as $E(\text{Na}_{x_1}\text{FPO})$, $E(\text{Na})$, and $E(\text{Na}_{x_2}\text{FPO})$, respectively, the molar enthalpy change can be expressed as

$$\Delta_r H_m = \left[E(\text{Na}_{x_2}\text{FPO}) - E(\text{Na}_{x_1}\text{FPO}) - (x_2 - x_1) E(\text{Na}) \right] \times F, \quad (2)$$

where F is the Faraday constant. According to the second law of thermodynamics, Gibbs free-energy change can be expressed by

$$\Delta_r G_m = \Delta_r H_m - T \Delta_r S_m = \Delta_r U_m + P \Delta_r V_m - T \Delta_r S_m. \quad (3)$$

Batteries are a condensed system where volume change and entropy change are negligible. In other words, Gibbs free-energy changes are mainly determined by internal energy change; this is easy to understand since according to the first law of thermodynamics:

$$\Delta U = Q + W. \quad (4)$$

The change in internal energy is equal to the sum of the heat absorbed (or released) and the work done by the external environment (or the change induced by the external environment). The essence of the battery is the conversion between chemical energy and electrical energy. Therefore, even if the battery absorbs heat from the outside, it cannot be used effectively. On the contrary, this kind of heat always causes detrimental

effects such as material deformation and electrolyte volatilization. After we neglect the volume change and entropy change terms, the universal relationship for battery is

$$\Delta_r G_m \approx \Delta_r H_m \approx \Delta_r U_m. \quad (5)$$

The Gibbs free energy is related to the potential by

$$\Delta_r G_m = -(x_2 - x_1) F V. \quad (6)$$

Therefore, according to Equations (2) and (6), the average intercalation potential of Na into offsto-NFPO can be determined by

$$V = -\frac{E(\text{Na}_{x_2}\text{FPO}) - E(\text{Na}_{x_1}\text{FPO})}{x_2 - x_1} + E(\text{Na}). \quad (7)$$

3 | RESULTS AND DISCUSSION

3.1 | Extending the solid-solution range

As shown in Figure 1A, offsto-NFPO and sto-NFPO (or its combined form, $\text{Na}_4\text{Fe}_2(\text{P}_2\text{O}_7)_2$) identical X-ray diffraction patterns, except for a slight peak shift, indicating that they belong to an isostructural system. sto-NFPO could be regarded as the lowest limit ($\alpha = 0$), and offsto-NFPO is the phase referring to the upper limit ($\alpha = 1$) in the general formula $\text{Na}_{4-\alpha}\text{Fe}_{2+\alpha/2}(\text{P}_2\text{O}_7)_2$. Therefore, a continuous solid solution with accessible α value ranging from 0 to 1 could actually

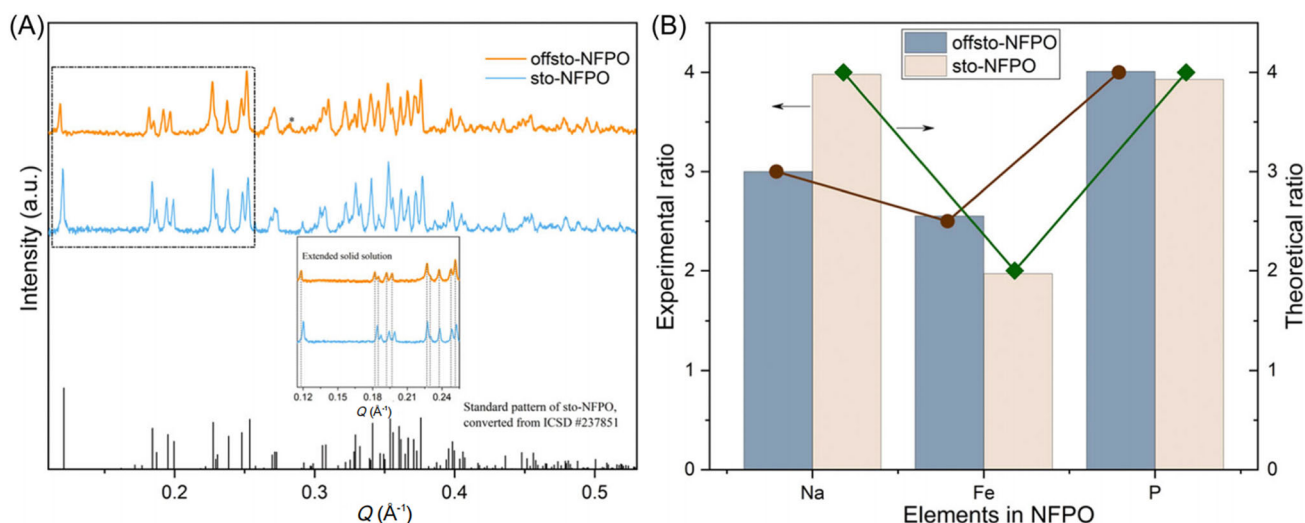


FIGURE 1 Extended solid solution range of $\text{Na}_{4-\alpha}\text{Fe}_{2+\alpha/2}(\text{P}_2\text{O}_7)_2$ with α value from 0 (for sto-NFPO) to 1 (for offsto-NFPO). (A) XRD patterns converted into Q values to show the shift in the layer distance. The inset shows the selected area. (B) Experimental and theoretical element ratio of ICP-OES measurements, normalized by sodium contents.

be obtained by changing the Na/Fe ratio while keeping the building blocks of P_2O_7 unchanged. This inference is rational due to the fact that in previous reports, $Na_{4-\alpha}Fe_{2+\alpha/2}(P_2O_7)_2$ ($2/3 \leq \alpha \leq 7/8$, or $0.667 \leq \alpha \leq 0.875$) and a sodium-rich ferric pyrophosphate, $Na_{3.64}Fe_{2.18}(P_2O_7)_2$ (with $\alpha = 0.36$) have been successfully prepared.²⁶ Compared to sto-NFPO, the diffraction peaks of offsto-NFPO gradually shift to small angle as the Na content increases (Figure S1), which means that the layers' distance is enlarged according to Bragg's law: $2d \times \sin\theta = n\lambda$.³⁵ Moreover, to ensure that no element loss occurred during the calcination process of the two samples, inductively coupled plasma-optical emission spectrometry (ICP-OES) is used and the result is shown in Figure 1B, in which the histograms show the experimental result normalized by sodium contents, while the lines show the theoretical data. The experimental ratios are 3.98: 1.97: 3.93 for sto-NFPO and 3.02: 2.55:4.01 for offsto-NFPO, close to their theoretical ratios of 4:2:4 and 3:2.5:4, respectively. Together with the XRD measurement, the ICP-OES results confirm that all elements are incorporated into the solid solution rather than form impurities because the Na, Fe, and P contents change synchronously with the targeted composition.

In addition, the morphology of the novel off-stoichiometric sample prepared using the simple ball-milling method, without the addition of costly graphene³⁶ or carbon nanotube²⁸ as in previous experiments, is characterized by field-emission scanning electron microscopy (FESEM), and results are shown in Figure S2. Due to the limitation of the ball milling method, neither uniform nor regular morphology can be found, even though characteristic features of nanoscale primary particles as well as enormous cavities that originated from the calcination process are observed. Such a configuration could induce nondiffusion-controlled reaction on specific active surface and cause numerous holes for the electrolyte to penetrate. The in situ carbon coating to improve the conductivity of the final product was formed during the high-temperature solid-state process, and its content, 9.81%, could be determined by gas chromatography and is shown in Figure S3. Besides, the carbon layer is indispensable to reinforce air stability as previous reports revealed that sodium iron pyrophosphate is sensitive to moisture and CO_2 .^{27,29,37} However, traces of nitrogen and moisture were also detected, which was aroused by exposure to air, as confirmed by the elemental analysis obtained using an energy-dispersive spectrometer under high vacuum as shown in Figure S4, where no nitrogen or other contaminated elements are detected.

Overall, a novel off-stoichiometric sodium ferric pyrophosphate is pyrophosphate, which is recognized

as the isostructural compound of stoichiometric $Na_2FeP_2O_7$, is formed, proving that $Na_{4-\alpha}Fe_{2+\alpha/2}(P_2O_7)_2$ forms in the solid solution, and the range can be extended from lower ($\alpha = 0$) to upper ($\alpha = 1$), providing more opportunities to explore new cathode materials for use in SIBs.

3.2 | Structural resolution and sodium-storage mechanism

Figure 2 shows the Rietveld refinement result of the X-ray diffraction pattern of offsto-NFPO. All characteristic reflections can be indexed to triclinic space group $P-1$. In particular, the sharp diffraction peaks indicate the high crystallinity of offsto-NFPO, while the absence of a peak from coated carbon suggests that the pyrolysis product of sucrose is in an amorphous form. The lattice parameters can be determined as follows: $a = 6.4223(2) \text{ \AA}$, $b = 9.4069(2) \text{ \AA}$, $c = 11.0038(3) \text{ \AA}$, $\alpha = 64.454(1)^\circ$, $\beta = 85.812(1)^\circ$, $\gamma = 72.919(1)^\circ$, and $V = 572.33 \text{ \AA}^3$. Interestingly, as shown in Table 1, two key points are noteworthy here: offsto-NFPO has shorter b and smaller volume compared to sto-NFPO. The decreasing b value would facilitate Na diffusion because two identical pathways are approximately parallel to the b axis, which means that the diffusion distance would be shortened.³² In terms of the volume change, the removal of Na^+ in sodiated sto-NFPO ($Na_2FeP_2O_7$; Na:Fe = 2:1) to desodiated sto-NFPO ($NaFeP_2O_7$; Na:Fe = 1:1) will induce a decrease in volume from 581.04 to 562.08 \AA^3 , while offsto-NFPO with a Na/Fe ratio of 1.2 has a volume smaller than

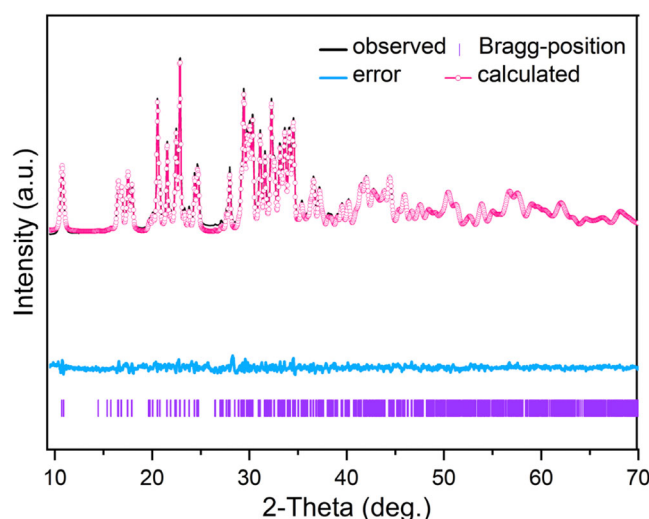


FIGURE 2 Rietveld refinement of powder XRD of offsto-NFPO with observed data points (black line), calculated pattern (red dotted line), difference curve (blue line), and Bragg positions (purple bars).

TABLE 1 Comparison of cell parameters of various NFPOs.

Sample	Space group	<i>a</i> (Å)	<i>b</i> (Å)	<i>c</i> (Å)	α (°)	β (°)	γ (°)	<i>V</i> (Å ³)
Na ₄ Fe ₂ (P ₂ O ₇) ₂ (stoichiometric)	<i>P</i> -1	6.4490	9.4825	10.9933	64.847	86.239	73.133	581.04
Na _{3.12} Fe _{2.44} (P ₂ O ₇) ₂ (off-stoichiometric)	<i>P</i> -1	6.4240	9.440	10.9810	64.77	86.21	73.13	575.19
Na ₃ Fe _{2.5} (P ₂ O ₇) ₂ (off-stoichiometric)	<i>P</i> -1	6.4223	9.4069	11.0038	64.454	85.812	72.919	572.33
NaFeP ₂ O ₇ (stoichiometric)	<i>P</i> -1	6.3297	9.4646	11.1000	62.611	83.290	72.24	562.08

sodiated sto-NFPO but larger than the desodiated one,³⁸ which is reasonable due to the intermediate Na/Fe ratio. Moreover, the volume of offsto-NFPO is also slightly smaller than 575.19 Å³ for another offsto phase Na_{3.12}-Fe_{2.44}(P₂O₇)₂ (indexed to ICSD #79312) with a Na/Fe ratio of 1.28, showing the consistency between volume and the Na/Fe ratio in sodium ferric pyrophosphate. Table 2 further summarizes the detailed crystallographic data. Unlike in the sodiated sto-NFPO where Fe and Na occupy separate sites, Na3 and Fe4, Na4 and Fe1 in offsto-NFPO show cation mixing, indicating that it is a new phase in sodium ferric pyrophosphate rather than a metastable phase generated by charging Na₂Fe-P₂O₇ to NaFeP₂O₇.

Detailed structural analysis of the new sodium phase was further carried out by structure resolution and theoretical calculation. The open channels formed by these layered structures of infinite [Fe₂P₄O₂₂]_∞ and [Fe₂P₄O₂₀]_∞ are conducive to the reversible insertion and extraction of sodium ions. The ball-wireframe model with Na and O highlighted in Figure 3A shows the relative size of each element in the form of ions. The P polyhedron highlighted in Figure 3B shows that all P exists in the form of [P₂O₇], which can be regarded as two [PO₄] tetrahedrons sharing one O atom corner. In contrast to the uniform configuration of P, Fe has two coordination forms as shown in Figure 3C: six-coordinated [FeO₆] octahedron for Fe1, Fe2, and Fe3 and edge-sharing tetrahedron [FeO₄] for Fe4, but this configuration has been ignored in all the related previous reports for analogs of Na_{4-α}Fe_{2+α/2}(P₂O₇)₂ families.²⁷⁻³¹ Due to the enhanced local electron density of cations, edge-sharing Fe octahedrons have higher electron conductivity than corner-sharing Fe octahedrons and the [P₂O₇] polyhedron.

The open framework built up with pyrophosphate has the potential to uptake Na and withstand repeated sodiation and desodiation. To better understand the sodium storage properties, DFT was therefore used to simulate the voltage profiles to better understand the structure–function relationship. Details of the inference process are provided in the above calculation section. The average intercalation potential of Na into offsto-NFPO can be determined using the following formula³⁹:

TABLE 2 Detailed crystallographic data for offsto-NFPO.

Atom	Symmetry	<i>x</i>	<i>y</i>	<i>z</i>	Occ.
Na1	2	0.1273	0.8989	0.5733	1
Na2	2	0.4014	0.1597	0.9068	1
Na3	1	0.5000	0.5000	0.5000	0.7291
Na4	2	-0.0306	0.1849	0.0036	0.7303
Fe1	2	-0.0306	0.1849	0.0036	0.2697
Fe2	2	0.3612	0.5256	0.2283	1
Fe3	2	0.2368	0.1176	0.2823	1
Fe4	2	0.8373	0.4504	0.3542	0.2709
P1	2	-0.0827	0.1383	0.6796	1
P2	2	0.2723	0.2187	0.5365	1
P3	2	0.5766	0.7277	-0.0693	1
P4	2	0.9119	0.4659	0.1333	1
O1	2	0.0643	0.3074	0.6229	1
O2	2	0.7015	0.5564	0.0411	1
O3	2	0.9428	-0.00373	0.7655	1
O4	2	0.7418	0.3517	0.6901	1
O5	2	0.0147	0.1319	0.8514	1
O6	2	0.4091	0.1319	0.8513	1
O7	2	0.3076	0.0588	0.5021	1
O8	2	0.5051	0.3034	0.4489	1
O9	2	0.6372	0.9329	-0.1133	1
O10	2	0.4543	0.7821	0.7543	1
O11	2	0.3832	0.6994	0.0521	1
O12	2	0.0424	0.5384	0.2251	1
O13	2	0.9268	0.3456	0.1977	1
O14	2	0.6507	0.4889	0.2317	1

$$V = -\frac{E(\text{Na}_{x_2}\text{FPO}) - E(\text{Na}_{x_1}\text{FPO})}{x_2 - x_1} + E(\text{Na}).$$

The voltage profiles were determined by using all stable phases from the pseudo-binary phase diagram of the sodiated and desodiated compounds,³⁹ and the

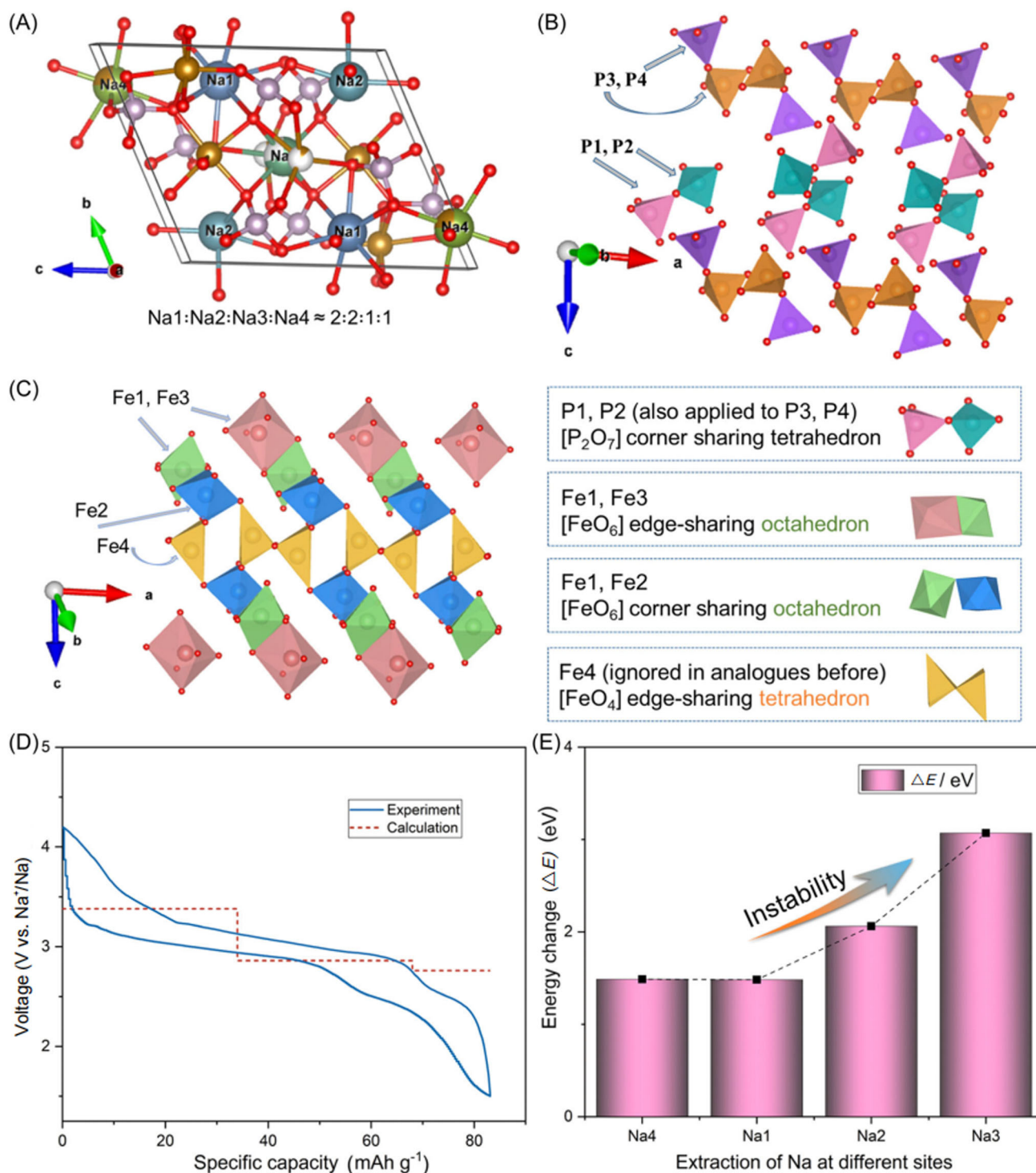


FIGURE 3 (A) The four Na sites and coordination environment highlighted in a ball-wireframe pattern. (B) Four-site P polyhedron and (C) Fe polyhedron configuration. Note that the Fe4 configuration has been ignored previously in the analogs of $\text{Na}_{4-\alpha}\text{Fe}_{2+\alpha/2}(\text{P}_2\text{O}_7)_2$ series. (D) Galvanostatic charge/discharge profiles of offsto-NFPO under 20 mA g^{-1} and the calculated average voltage in each region. (E) Energy change of crystal structures when Na ions at different sites are extracted.

results are shown in Figure 3D. Note that the hysteresis between the simulated value and the experimental voltage is reasonable as polarizations arising from diffusion, charge transfer, and intrinsic ohmic resistance are inevitable.⁴⁰ DFT calculation indicates that the

extraction of Na ions follows the sequence of Na4, Na1, and Na2 during charging and reversed order during discharging, which is in good agreement with electrochemical testing. Based on the pseudo-binary phase diagram, the ratio of Na ions extracted or inserted

is 0.37: 0.91: 1.11, which is consistent with the structure–function relationship, where the Na ratio in different sites is 1:2:2 as shown in Figure 3A. However, there is still some deviation between the two ratios, which may be due to the following factors: the Na4 site is partially occupied by Fe, which prevents the extraction of all Na, and Na at different sites may have different movement orders instead of a strict theoretical order. The movement order of Na ions can be re-evaluated by another method that unstable configurations will be generated when Na ions at different sites are extracted. As shown in Figure 3E, the energy change of above-mentioned unstable configurations compared with the initial structure gradually increases and reaches the maximum for Na3, confirming again that this is the most unstable configuration, consistent with the simulated charge–discharge curves. Therefore, both the

structure–function relationship and the DFT calculation indicate that the extraction sequence of sodium can be described as follows: Na4 and Na1 are extracted first, followed by Na₂, while Na3 at the core of structure has the highest diffusive activation energy.

To gain more insights into the kinetics and quantitatively verify the Na⁺ diffusion behavior in the off-stoichiometric structure, the CI-NEB of density functional theory calculations was implemented. The principle involves the insertion of a specified number of points and the creation of a proper path for ion movement from the initial to the final state. The “saddle point” or the transition state structure within the whole migration process will be checked when the structural energy on the path increases to the maximum. We found that diffusion of Na⁺ ions preferentially proceeds via three very plausible 1D pathways as shown in Figure 4A–C: for

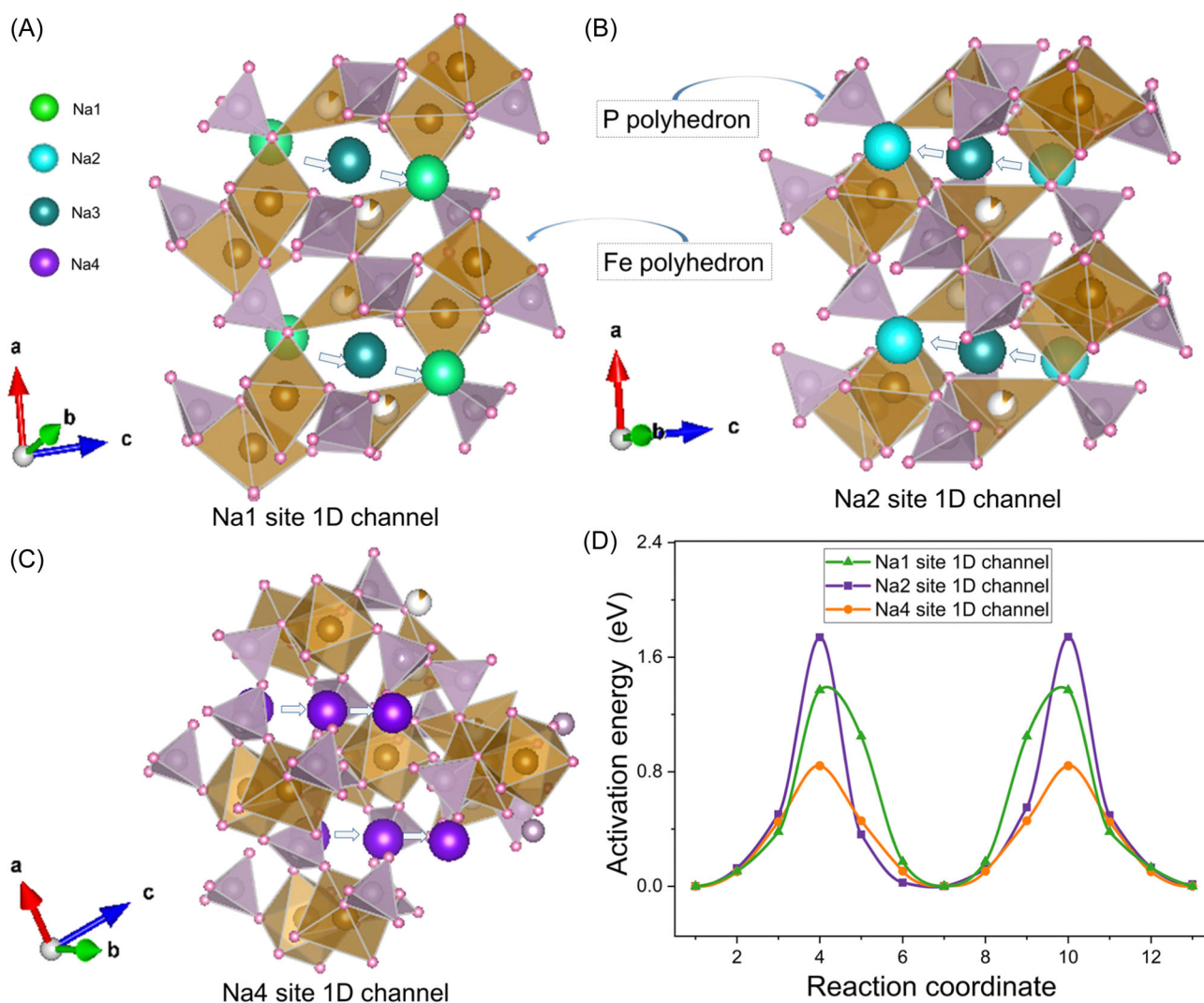


FIGURE 4 Three Na-ion diffusion channels of (A) path I: Na1 site 1D channel paralleling axis *b*, (B) path II: Na2 site 1D channel approximately paralleling the *bc* plane, and (C) path III: Na4 site 1D channel nearly perpendicular to the *ac* plane. (D) Corresponding activation energy from DFT calculations.

path I, Na1 site 1D channel paralleling axis *b*, for path II, Na2 site 1D channel approximately paralleling the *bc* plane, and for path III, Na4 site 1D channel nearly perpendicular to the *ac* plane. It is noteworthy that only two feasible paths were found in another offstoichiometric sodium ferric pyrophosphate $\text{Na}_{3.32}\text{Fe}_{2.34}(\text{P}_2\text{O}_7)_2$ in a previous report.³² The results of the calculation are shown in Figure 4D, and more information of the parameters can be found in the above calculation section. By comparing the energy barrier along the reaction coordinate, path III has the lowest energy barrier, while path II has the highest energy barrier among the three diffusion channels. Therefore, the movement of Na^+ in path III occurs preferentially, followed by path I and path II when charging takes place, in agreement with results of the thermodynamics calculation presented in Figure 3D,E. The movement of ions will inevitably cause deviation from the ground state, and this is also the fundamental reason why we need to charge the electrode to provide enough energy.

3.3 | Sodium-storage performance

Due to its simple composition and feasible structure, the tentative application of novel offsto-NFPO as a cathode material in SIBs was investigated. The offsto-NFPO cast on an Al foil cut into small slices which acted as the working electrode in a 2032 type coin cell with Na metal as the counter electrode. Figure 5A shows that the offsto-NFPO/C electrode could deliver an appreciable discharge capacity of 83 mAh g^{-1} under galvanostatic charge and discharge process at a current density of 20 mA g^{-1} . The negligible change in the capacity and overlapped charge/discharge curves during the first to subsequent four cycles indicates excellent reversibility for Na^+ insertion and extraction in the framework. Notably, a small polarization gap of 0.15 V between average charge/discharge also confirmed the high kinetics. Further measurement indicated that this cathode could show an average operation voltage of 2.90 V, which is higher than that of 2.70 V of olivine⁴¹ and 2.10 V of amorphous²⁰ NaFePO_4 due to the stronger inductive effect of pyrophosphate than phosphate. In both the first and following cycles, the charging profiles show apparently two distinct regions of different electrochemical activity: the low-voltage region around 2.5 V with a short slope segment and the high-voltage region above 3 V with a long slope segment. Indeed, as shown in the CV test in Figure 5B, a symmetrical pair of peaks around 2.5 V and three peaks between 3 and 3.5 V were recorded, corresponding to the single-phase reaction and a series of two-

phase reactions,²⁴ respectively. Under the Na-deficient condition, the peak split into multiple minor peaks; this is a common phenomenon that occurs in many other polyanionic cathodes.^{11,12,19}

Subsequently, the kinetics of Na-ion insertion/deinsertion is further studied by CV at various scan rates. The CV curves in Figure 5C maintain the same shape with a subtle shift of redox peaks for continuous increase in the scan rate. The linear relationship in Figure 5D between the peak currents and the square root of the scanning rate ($v^{1/2}$) indicates that the Na-storage reaction in offsto-NFPO is a diffusion-controlled process. Therefore, the apparent diffusion coefficient of sodium ions (\tilde{D}_{Na^+}) can be calculated according to the Randles-Sevcik equation^{19,42}:

$$I_p = 2.69 \cdot 10^5 \cdot n^{3/2} \cdot A \cdot \sqrt{\tilde{D}_{\text{Na}^+}} \cdot C_{\text{Na}^+}^* \cdot \sqrt{v},$$

where I_p is the peak current (A), n is the number of electrons transfer per species in the reaction, A is the electrode area (1.44 cm^2), $C_{\text{Na}^+}^*$ is the bulk concentration of the sodium ion in the electrode (calculated to be $0.0175 \text{ mol cm}^{-3}$; the calculation process is described in Figure S5), and v is the scan rate (V s^{-1}). The apparent electrochemical diffusion coefficients can thereby be calculated, supposing that Na values are considered to be constant in the whole phase transition regime and the system is homogeneous.⁴² The apparent diffusion coefficients of the Na^+ ions in the solid matrix during the desodiation process are calculated to be 5.52×10^{-13} and $5.36 \times 10^{-12} \text{ cm}^2 \text{ s}^{-1}$ for i_{a1} and i_{a2} , respectively, while the values in the sodiation process are 3.51×10^{-12} and $3.84 \times 10^{-12} \text{ cm}^2 \text{ s}^{-1}$ for i_{c1} and i_{c2} , respectively. These values are comparable with those of sto-NFPO decorated with a meticulously designed carbon matrix and expanded graphite,⁴³ comparable with many other sodium uptake hosts.^{44–46} This superior kinetics could also be observed in the comparative CV curves of sto-NFPO and offsto-NFPO in Figure S6 where larger polarization is observed in sto-NFPO. The rate performance of the electrode was investigated and is shown in Figure S7. The offsto-NFPO electrode demonstrates excellent power capability, which shows negligible capacity degradation when the current density is increased from 50 to 400 mA g^{-1} , with 73, 64, and 51 mAh g^{-1} at current densities of 800, 1200, and 1600 mA g^{-1} for 10 cycles, respectively. A good capacity of 72 mAh g^{-1} could be recovered when current was reversed to 20 mA g^{-1} , indicating a strong tolerance for rapid Na-ion insertion/extraction. In comparison, the stoichiometric sample shows rapid degradation when the current increased and only 31 mAh g^{-1} could be harvested at the same maximal current. Moreover, the long-life cycling

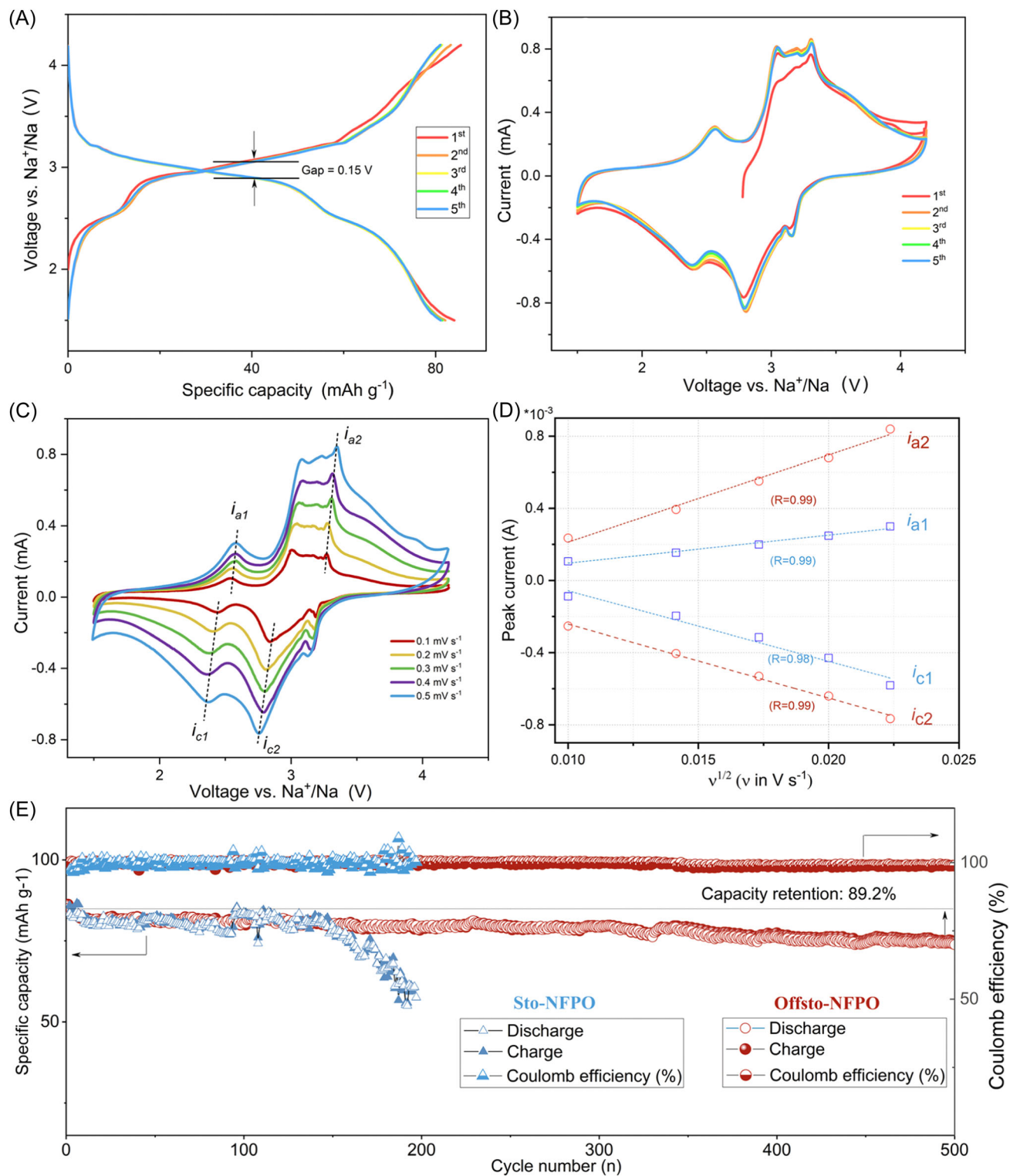


FIGURE 5 Electrochemical reversibility in sodium-ion batteries. (A) Galvanostatic charge and discharge profiles at a current density of 20 mA g^{-1} and (B) the first to fifth CV curve at a scan rate of 0.5 mV s^{-1} . (C) CV curves at an increased scan rate from 0.1 to 0.5 mV s^{-1} . (D) Corresponding relationship of peak currents to the square root of scan rates (symbols show the measured data, while the dashed lines show the fitted results). (E) Long-term cycling performances at 20 mA g^{-1} for both sto-NFPO and offsto-NFPO.

performances of sto-NFPO and offsto-NFPO were measured under the same conditions. As shown in Figure 5E, sto-NFPO shows a rapid capacity decay to 52 mAh g^{-1} even with less than 200 cycles. In comparison, for the offsto-NFPO electrode, a reversible capacity of 70 mAh g^{-1} is reached even 500 cycles in a prolonged measurement process with a current density of 20 mA g^{-1} , showing excellent retention of 89.2% compared with the initial cycle, confirming the reinforced structure stability and intrinsic merits of off-stoichiometric polyanionic frameworks when the solid solution range is extended.

4 | CONCLUSION

Overall, extending the solid solution range of $\text{Na}_{4-\alpha}\text{Fe}_{2+\alpha}/_2(\text{P}_2\text{O}_7)_2$ to $\alpha = 1$ enables the generation of a novel off-stoichiometric sodium ferric pyrophosphate. Structure resolution, theoretical calculation, and sodium storage properties are comprehensively studied to disclose its structure–function relationship when used as a sodium uptaking cathode. The as-prepared off-stoichiometric electrode shows electrochemical activity in SIBs with a highly reversible discharge capacity of 83 mAh g^{-1} , a remarkable retention of 89.2% over 500 cycles, and high rate capability. This work successfully validated promising phase that is concealed inside of extending solid solution range of sodium ferric pyrophosphate, providing an alternative pathway for the invention of a stable and high-reversible cathode for SIBs.

ACKNOWLEDGMENTS

This work was financially supported by the National Natural Science Foundation of China (21972108, U20A20249, U22A20438), the Changzhou Science and Technology Bureau (CM20223017) and Innovation and Technology Commission (ITC) of Hong Kong, The Innovation & Technology Fund (ITF) with Project No. ITS/126/21.

CONFLICT OF INTEREST STATEMENT

The authors declare that there are no conflicts of interests.

ORCID

Xiangjun Pu  <http://orcid.org/0000-0001-8953-4209>

Kunran Yang  <http://orcid.org/0000-0002-7777-5547>

Zhongxue Chen  <http://orcid.org/0000-0002-1526-7336>

Yuliang Cao  <http://orcid.org/0000-0001-6092-5652>

REFERENCES

- Zhang J, Cui C, Wang P-F, et al. "Water-in-salt" polymer electrolyte for Li-ion batteries. *Energy Environ Sci.* 2020;13(9):2878-2887.
- Zhang J, Wang P-F, Bai P, et al. Interfacial design for a 4.6 V high-voltage single-crystalline LiCoO_2 cathode. *Adv Mater.* 2022;34(8):2108353.
- Qiu S, Xiao L, Sushko ML, et al. Manipulating adsorption-insertion mechanisms in nanostructured carbon materials for high-efficiency sodium ion storage. *Adv Energy Mater.* 2017;7(17):1700403.
- Hong Z, Zhen Y, Ruan Y, et al. Rational design and general synthesis of S-doped hard carbon with tunable doping sites toward excellent Na-ion storage performance. *Adv Mater.* 2018;30(29):1802035.
- Pu X, Wang H, Zhao D, et al. Recent progress in rechargeable sodium-ion batteries: toward high-power applications. *Small.* 2019;15(32):1805427.
- Chen Z, Yuan T, Pu X, et al. Symmetric sodium-ion capacitor based on $\text{Na}_{0.44}\text{MnO}_2$ nanorods for low-cost and high-performance energy storage. *ACS Appl Mater Interfaces.* 2018;10(14):11689-11698.
- Yuan T, Zhang J, Pu X, et al. Novel alkaline $\text{Zn}/\text{Na}_{0.44}\text{MnO}_2$ dual-ion battery with a high capacity and long cycle lifespan. *ACS Appl Mater Interfaces.* 2018;10(40):34108-34115.
- Li H, Liu S, Wang H, et al. Improved sodium storage performance of $\text{Na}_{0.44}\text{MnO}_2$ cathode at a high temperature by Al_2O_3 coating. *Acta Phys Chim Sin.* 2019;35(12):0001-0009.
- Qian J, Zhou M, Cao Y, Ai X, Yang H. Nanosized $\text{Na}_4\text{Fe}(\text{CN})_6/\text{C}$ composite as a low-cost and high-rate cathode material for sodium-ion batteries. *Adv Energy Mater.* 2012;2(4):410-414.
- Pu X, Rong C, Tang S, et al. Zero-strain $\text{Na}_4\text{Fe}_7(\text{PO}_4)_6$ as a novel cathode material for sodium-ion batteries. *Chem Commun.* 2019;55(61):9043-9046.
- Yuan T, Wang Y, Zhang J, et al. 3D graphene decorated $\text{Na}_4\text{Fe}_3(\text{PO}_4)_2(\text{P}_2\text{O}_7)$ microspheres as low-cost and high-performance cathode materials for sodium-ion batteries. *Nano Energy.* 2019;56:160-168.
- Zhao A, Yuan T, Li P, et al. A novel Fe-defect induced pure-phase $\text{Na}_4\text{Fe}_{2.91}(\text{PO}_4)_2\text{P}_2\text{O}_7$ cathode material with high capacity and ultra-long lifetime for low-cost sodium-ion batteries. *Nano Energy.* 2022;91:106680.
- Wang P-F, You Y, Yin Y-X, Guo Y-G. Layered oxide cathodes for sodium-ion batteries: phase transition, air stability, and performance. *Adv Energy Mater.* 2018;8(8):1701912.
- Choi JW, Aurbach D. Promise and reality of post-lithium-ion batteries with high energy densities. *Nat Rev Mater.* 2016;1(4):16013.
- Wang B, Han Y, Wang X, et al. Prussian blue analogs for rechargeable batteries. *iScience.* 2018;3:110-133.
- Fang Y, Liu Q, Xiao L, et al. A Fully sodiated NaVOPO_4 with layered structure for high-voltage and long-lifespan sodium-ion. *Chem.* 2018;4(5):1167-1180.
- Fang Y, Zhang J, Xiao L, Ai X, Cao Y, Yang H. Phosphate framework electrode materials for sodium ion batteries. *Adv Sci.* 2017;4(5):1600392.
- Fang Y, Xiao L, Chen Z, Ai X, Cao Y, Yang H. Recent advances in sodium-ion battery materials. *Electrochem Energy Rev.* 2018;1(3):294-323.
- Pu X, Wang H, Yuan T, et al. $\text{Na}_4\text{Fe}_3(\text{PO}_4)_2(\text{P}_2\text{O}_7)/\text{C}$ nanospheres as low-cost, high-performance cathode material for sodium-ion batteries. *Energy Storage Mater.* 2019;22:330-336.

20. Liu Y, Zhang N, Wang F, Liu X, Jiao L, Fan LZ. Approaching the downsizing limit of maricite NaFePO_4 toward high-performance cathode for sodium-ion batteries. *Adv Funct Mater.* 2018;28(30):1801917.
21. Tang W, Song X, Du Y, et al. High-performance NaFePO_4 formed by aqueous ion-exchange and its mechanism for advanced sodium ion batteries. *J Mater Chem A.* 2016;4(13):4882-4892.
22. Lu J, Chung SC, Nishimura S-i, Yamada A. Phase diagram of olivine Na_xFePO_4 ($0 < x < 1$). *Chem Mater.* 2013;25(22):4557-4565.
23. Barpanda P, Ye T, Nishimura S, et al. Sodium iron pyrophosphate: a novel 3.0V iron-based cathode for sodium-ion batteries. *Electrochem Commun.* 2012;24:116-119.
24. Kim H, Shakoor RA, Park C, et al. $\text{Na}_2\text{FeP}_2\text{O}_7$ as a promising iron-based pyrophosphate cathode for sodium rechargeable batteries: a combined experimental and theoretical study. *Adv Funct Mater.* 2013;23(9):1147-1155.
25. Song HJ, Kim KH, Kim JC, Hong SH, Kim DW. Superior sodium storage performance of reduced graphene oxide-supported $\text{Na}_{3.12}\text{Fe}_{2.44}(\text{P}_2\text{O}_7)_2/\text{C}$ nanocomposites. *Chem Commun.* 2017;53(67):9316-9319.
26. Shen B, Xu M, Niu Y, et al. Sodium-rich ferric pyrophosphate cathode for stationary room-temperature sodium-ion batteries. *ACS Appl Mater Interfaces.* 2018;10(1):502-508.
27. Ha K-H, Woo SH, Mok D, et al. $\text{Na}_{4-\alpha}\text{M}_{2+\alpha/2}(\text{P}_2\text{O}_7)_2$ ($2/3 \leq \alpha \leq 7/8$, $\text{M} = \text{Fe}, \text{Fe}_{0.5}\text{Mn}_{0.5}$, Mn): a promising sodium ion cathode for na-ion batteries. *Adv Energy Mater.* 2013;3(6):770-776.
28. Niu Y, Xu M, Cheng C, et al. $\text{Na}_{3.12}\text{Fe}_{2.44}(\text{P}_2\text{O}_7)_2$ /multi-walled carbon nanotube composite as a cathode material for sodium-ion batteries. *J Mater Chem A.* 2015;3(33):17224-17229.
29. Chen CY, Matsumoto K, Nohira T, Hagiwara R. Full utilization of superior charge-discharge characteristics of $\text{Na}_{1.56}\text{Fe}_{1.22}\text{P}_2\text{O}_7$ positive electrode by using ionic liquid electrolyte. *J Electrochem Soc.* 2014;162(1):A176-A180.
30. Niu Y, Xu M, Dai C, Shen B, Li CM. Electrospun graphene-wrapped $\text{Na}_{6.24}\text{Fe}_{4.88}(\text{P}_2\text{O}_7)_4$ nanofibers as a high-performance cathode for sodium-ion batteries. *Phys Chem Chem Phys.* 2017;19(26):17270-17277.
31. Liu Q, Hu Z, Chen M, et al. Multiangular rod-shaped $\text{Na}_{0.44}\text{MnO}_2$ as cathode materials with high rate and long life for sodium-ion batteries. *ACS Appl Mater Interfaces.* 2017;9(4):3644-3652.
32. Chen M, Chen L, Hu Z, et al. Carbon-coated $\text{Na}_{3.32}\text{Fe}_{2.34}(\text{P}_2\text{O}_7)_2$ cathode material for high-rate and long-life sodium-ion batteries. *Adv Mater.* 2017;29(21):1605535.
33. Momma K, Izumi F. VESTA 3 for three-dimensional visualization of crystal, volumetric and morphology data. *J Appl Crystallogr.* 2011;44(6):1272-1276.
34. Boucher F, Gaubicher J, Cuisinier M, Guyomard D, Moreau P. Elucidation of the $\text{Na}_{2/3}\text{FePO}_4$ and $\text{Li}_{2/3}\text{FePO}_4$ intermediate superstructure revealing a pseudouniform ordering in 2D. *J Am Chem Soc.* 2014;136(25):9144-9157.
35. Fang Y, Chen Z, Xiao L, Ai X, Cao Y, Yang H. Recent progress in iron-based electrode materials for grid-scale sodium-ion batteries. *Small.* 2018;14(9):1703116.
36. Niu Y, Xu M, Bao SJ, Li CM. Porous graphene to encapsulate $\text{Na}_{(6.24)}\text{Fe}_{(4.88)}(\text{P}_2\text{O}_7)_4$ as composite cathode materials for Na-ion batteries. *Chem Commun.* 2015;51(66):13120-13122.
37. Liu B, Zou Y, Chen S, et al. Seaweed-derived synthesis of $\text{Na}_{3.12}\text{Fe}_{2.44}(\text{P}_2\text{O}_7)_2/\text{r-GO}$ aerogels as air stable cathode materials for sodium-ion batteries. *Chem Eng J.* 2019;365:325-333.
38. Barpanda P, Liu G, Ling CD, et al. $\text{Na}_2\text{FeP}_2\text{O}_7$: a safe cathode for rechargeable sodium-ion batteries. *Chem Mater.* 2013;25(17):3480-3487.
39. Guo X, Wang Z, Deng Z, Wang B, Chen X, Ong SP. Design principles for aqueous Na-ion battery cathodes. *Chem Mater.* 2020;32(16):6875-6885.
40. Pu X, Zhao D, Fu C, et al. Understanding and calibration of charge storage mechanism in cyclic voltammetry curves. *Angew Chem Int Ed.* 2021;133(39):21480-21488.
41. Fang Y, Liu Q, Xiao L, Ai X, Yang H, Cao Y. High-performance olivine NaFePO_4 microsphere cathode synthesized by aqueous electrochemical displacement method for sodium ion batteries. *ACS Appl Mater Interfaces.* 2015;7(32):17977-17984.
42. Tang K, Yu X, Sun J, Li H, Huang X. Kinetic analysis on LiFePO_4 thin films by CV, GITT, and EIS. *Electrochim Acta.* 2011;56(13):4869-4875.
43. Zeng L, Li F, Xu X, et al. A scalable approach to $\text{Na}_2\text{FeP}_2\text{O}_7@$ -Carbon/expanded graphite as a low-cost and high-performance cathode for sodium-ion batteries. *ChemElectroChem.* 2020;7(18):3874-3882.
44. Sato T, Yoshikawa K, Zhao W, et al. Efficient stabilization of Na storage reversibility by Ti integration into O'3-type NaMnO_2 . *Energy Mater Adv.* 2021;2021:9857563.
45. Zhang L-L, Wei C, Fu X-Y, et al. Ternary Ni-based Prussian blue analogue with superior sodium storage performance induced by synergistic effect of Co and Fe. *Carbon Energy.* 2021;3(5):827-839.
46. Chen T, Ouyang B, Fan X, Zhou W, Liu W, Liu K. Oxide cathodes for sodium-ion batteries: designs, challenges, and perspectives. *Carbon Energy.* 2022;4(2):170-199.

SUPPORTING INFORMATION

Additional supporting information can be found online in the Supporting Information section at the end of this article.

How to cite this article: Pu X, Yang K, Pan Z, et al. Extending the solid solution range of sodium ferric pyrophosphate: off-stoichiometric $\text{Na}_3\text{Fe}_{2.5}(\text{P}_2\text{O}_7)_2$ as a novel cathode for sodium-ion batteries. *Carbon Energy.* 2024;6:e449. doi:10.1002/cey2.449